An exploratory rehearsal on AIE dots assisted NIR-II fluorescence non-human primates imaging

Zhe Feng[1,6], Siyi Bai[2,6], Ji Qi[3,6], Chaowei Sun[1], Yuhuang Zhang[1], Xiaoming Yu[4], Huwei Ni[1], Di Wu[5], Xiaoxiao Fan[5], Dingwei Xue[5], Junyi Gong[3], Peifa Wei[3], Mubin He[1], Jacky W. Y. Lam[3], Xinjian Li[2], Ben Zhong Tang[3]*, Lixia Gao[2]*, Jun Qian[1,5]*.

[1]State Key Laboratory of Modern Optical Instrumentations, Centre for Optical and Electromagnetic Research, College of Optical Science and Engineering, International Research Center for Advanced Photonics, Zhejiang University, Hangzhou 310058, China

[2]Department of Neurology of the Second Affiliated Hospital, Interdisciplinary Institute of Neuroscience and Technology, Zhejiang University School of Medicine, Key Laboratory for Biomedical Engineering of Ministry of Education, College of Biomedical Engineering and Instrument Science, Zhejiang University, Hangzhou 310027, China

[3]Department of Chemistry, The Hong Kong Branch of Chinese National Engineering Research Center for Tissue Restoration and Reconstruction, Institute for Advanced Study and Department of Chemical and Biological Engineering and Institute of Molecular Functional Materials, The Hong Kong University of Science and Technology, Clear Water Bay, Kowloon, Hong Kong, China.

[4]Women's Hospital, Zhejiang University School of Medicine, Hangzhou 310006, China

[5]Sir Run-Run Shaw Hospital, Zhejiang University School of Medicine, Hangzhou 310016, China

[6]These authors contributed equally: Zhe Feng, Siyi Bai, Ji Qi.

Correspondence and requests for materials should be addressed to J.Q. (J. Qian) (E-mail: qianjun@zju.edu.cn) or to L.G. (E-mail: lxgao10@zju.edu.cn) or to B.Z.T. (E-mail: tangbenz@ust.hk)

Abstract

Booming AIE universe has set off an upsurge in recent years, driving much innovation in academic, industrial and medical world. Superb reliability and biocompatibility equip AIE dots with tremendous potential for fluorescence bioimaging and even clinical translation. The utilization on non-human primates imaging are vital for AIE dots assisted clinical theranostics, which still remains unexplored yet. Additionally, fluorescence bioimaging in second near-infrared window (NIR-II, 900-1700 nm) is widely recognized as an effective technology for deep-penetration mammals optical imaging. Here, we designed a novel AIEgen with a large molar extinction coefficient of ~5×10^4 mM^{-1} cm^{-1} at ~770 nm and the PEGylated AIE dots possessed an extremely high NIR-II photoluminescence quantum yield (PLQY) as 13.6%, exhibiting bright fluorescence beyond 1100 nm and even 1500 nm (near-infrared IIb, NIR-IIb). Assisted by the AIE dots, large-depth cerebral vasculature

(beyond 600 μm) as well as real-time blood flowing were monitored through the skull and high-spatial-frequency non-invasive NIR-IIb (beyond 1500 nm) imaging gave a precise presentation of gastrointestinal tract in marmosets. Importantly, after intravenous or oral administration, the definite excretion of AIE dots from the body was demonstrated. It was the first attempt for AIE dots assisted NIR-II fluorescence imaging in non-human primates and we wished this work could promote the development of AIE dots for clinical application.

Main

Exogenous photoluminescent organic dyes are widely perceived with good biocompatibility and have been extensively used in biopharmaceutics and imaging[1-3]. However, luminophores always experience some effects of emission quenching, partially or completely in the state of aggregation, impeding the progress of some specific applications[4]. In 2001, the uncommon luminogen system noted as aggregation-induced emission (AIE) by our group broke down the captivity of Förster's discovery of the aggregation-caused quenching (ACQ)[5], which brought a new wonderland for organic fluorophores. The intrinsic tendency to form aggregates in concentrated solutions or the solid state actively promotes the emission intensity of the fluorophores with AIE characteristics. Years of unremitting exploration has accumulated design experience of diverse AIEgens and shaped plentiful innovated applications for stimuli sensing[6-9], optoelectronic systems[10-12], molecular detection[13-15], bio-imaging[16, 17] and so on. Taking advantage of the AIE dots with high resistance to photobleaching and excellent reliability, multifarious specific bio-sensing modes, including bio-imaging, launched on a grand[16, 18, 19].

The highly successful application strategies to employ AIEgens for fluorescence imaging in mice have already proven feasible by us and other groups[16, 20-29]. However, doubtless the utilization in non-human primates is an essential step for AIE dots to advance clinically. Non-human primates with a strong homology and similarity of organizational structure and physiological functions to human beings[30, 31] have been considered to be ideal laboratory animal models for the studies of life science[32, 33] and pre-clinical studies of new drugs[34]. The special columnar, modular and laminar structure of the cortex in non-human primates demonstrates a closer metabolic coupling between neurons, glial cells[35], and cerebral vasculature[36, 37], and may reflect the cytoarchitectonic and functional features of the cortex[38], which is distinguished from the cortex of rodents. Additionally, the gastrointestinal (GI) structure of non-human primates simulates that of human beings realistically[39, 40], which greatly facilitates the researches about GI disorders. However, there are still few investigations whatsoever of improvement on AIE dots towards non-human primates imaging at present, attributing to the rigorous safety requirements and the high clarification complexity of information at large tissue-depth in non-human primates.

Fluorescence imaging has been widespread recognized in biological fundamental research and clinical applications in the light of its high sensitivity, non-invasiveness

and free-radiation[3, 41-43]. Given the suppressed tissue-scattering and diminished autofluorescence, fluorescence bio-imaging in the second near-infrared region (NIR-II, 900–1700 nm) allows the precise visualization of details throughout some thick tissues in mammals with high signal-to-background ratio and sharp spatial resolution[44-50]. It was demonstrated that there existed a great improvement in imaging quality beyond 900 nm or even 1500 nm compared to the traditional NIR-I fluorescence imaging (780-900 nm), thereby gifting a credible approach for deep-penetration non-human primates imaging *in vivo*[51-53]. Importantly, the biosafety concerns for non-human primates should also been taken into serious consideration, which could be of vital importance for further clinical application. Recently, clinically approved indocyanine green assisted NIR-II fluorescence imaging has been successfully conducted in macaque monkeys[54]. Hence, longer emission wavelength, brighter emission intensity and biological excretion constitute the three harsh demand for new AIE dots especially for imaging performed at non-human primate models. Moreover, it should be noted that low doses might allow the rapid excretion from the organics but also putting forward higher requirements for the dots' emission intensity at the same time.

Herein, we designed a novel NIR-II AIEgen named as OTPA-BBT with a large molar extinction coefficient of ~5×10^4 mM^{-1} cm^{-1} at ~770 nm. PEGylated AIE dots with an extremely high NIR-II photoluminescence quantum yield (PLQY), measured as 13.6%, was verified to emit ultra-bright luminescence beyond 1100 nm and even beyond 1500 nm (near-infrared IIb, NIR-IIb). NIR-II fluorescence through-skull large-depth cerebrovascular microscopic imaging and NIR-IIb fluorescence noninvasive GI imaging in non-human primates were well conducted for the first time by aid of the novel AIE dots at incredibly low doses (2 mg kg^{-1} for intravenous injection and 15 mg kg^{-1} for feeding). Notably, the excretion of dots in hepatobiliary and gastro-intestinal pathway in non-human primates and rodents was substantiated drawing support from the sophisticated NIR-II fluorescence imaging technology. Thus, the potential application of the AIE dots on large animals have been significantly pushed ahead and the eventual goal of clinical translation would be possibly immensely accelerated.

Molecular design and photophysical properties

The fluorescence brightness of an emitter is determined by the extinction coefficient (ε) and PLQY, in which the former one reflects the ability of a chromophore to attenuate light at a given wavelength and the later expresses the efficiency to give out light via radiative decay. Therefore, it is of great interest to develop fluorophores with simultaneously high ε and PLQY, yet these two parameters seem contrary with each other. From the molecular structure point of view, high ε usually requires a planar conformation to allow for efficient π-orbital overlap and oscillator strength, while high PLQY is favourable in twisted structures to avoid the notorious ACQ effect. To solve this issue, in this work, we propose a kind of molecule possessing a highly conjugated core structure with several twisting phenyl rings. The planar core unit with good conjugation would enable efficient electron transition, and the substituted benzene rotors are expected to inhibit intermolecular π-π stacking and afford AIE signature. To

realize low bandgap and long-wavelength excitation/emission, a strong donor-acceptor (D-A) type compound was built, in which octyloxy-substituted triphenyl amine (OTPA) and benzobisthiadiazole (BBT) served as the electron-donating and -withdrawing moieties, respectively. The detailed syntheses and characterizations of OTPA-BBT and the intermediates are presented in the **Supplementary Fig. 1-8**. Density functional theory (DFT) calculation reveals that OTPA-BBT has a relatively planar core structure, and the peripheral phenyl derivatives are highly twisted. As displayed in **Fig. 1a**, the electron density of the highest occupied molecular orbital (HOMO) is distributed on both the donor and acceptor moieties, whereas the lowest unoccupied molecular orbital (LUMO) is mainly localized on the electron-withdrawing BBT unit, indicating D-A characteristics with strong intramolecular charge transfer.

The absorption spectrum of OTPA-BBT in THF is presented in **Fig. 1b**. Interestingly, the compound exhibits broad absorption in NIR spectral region with a high molar absorption coefficient of ~5×10^4 M^{-1} cm^{-1} at ~770 nm, which is among the highest values of organic chromophores and advantageous for efficient light excitation. The oscillator strength (f) expresses the probability of a molecule to transit between different energy levels, representing an indicator of excitation ability. The f value of OTPA-BBT from HOMO to LUMO is calculated to be as high as 0.76, which suggests high electron transition possibility and explains the high ε value. We next investigated the photoluminescence (PL) properties in different aggregate states. PL intensity of OTPA-BBT gradually decreases by increasing the water fraction (f_w) in THF/H_2O mixture to 30%, which is probably due to the twisted intramolecular charge transfer (TICT) effect in high polarity environment. Then the emission intensifies when further increasing f_w to 90%, representing remarkable AIE signature (**Fig. 1c, d**). Moreover, the pronounced bathochromic shift of maximal PL wavelength in high water fraction indicates the formation of aggregate and thus the polarity of microenvironment declines.

Characterization and *in vivo* biodistribution of dots

The AIEgens were then encapsulated into organic nanoparticles by nanoprecipitation using US Food and Drug Administration (FDA)-approved F-127 (**Fig. 2a**). The amphiphilic block copolymers could ameliorate the hydrophilicity and biocompatibility of luminescent probes. On the flip side, the matrix aggregated the AIEgens and the intramolecular motions was moderated by the pinning among the molecules. As shown in **Fig. 2b**, the micellar systems were uniform with a narrow size distribution (~27.7 nm) from dynamic light scattering (DLS) and transmission electron microscopy (TEM). Taking IR-26 in dichloroethane as a reference (with a nominal PLQY = 0.5%), the NIR-II photoluminescence quantum yield of the AIE dots was determined to be 13.6% (**Supplementary Fig. 9**). Due to the large absorption, high PLQY in NIR-II region and the strong emission in the aggregate state, the AIE dots showed bright NIR-II fluorescence. The photoluminescence excitation (PLE) mapping was performed on the AIE dots and demonstrated the excitation–emission relationships which brought us an in-depth understanding about the optical properties, as shown in

Fig. 2c. Furthermore, the integral spectrum of the fluorescence intensity in **Fig. 2d** intuitively revealed the considerable emission and the discrepancy on the ordinate represented the total fluorescence intensity beyond 1100 nm and 1500 nm. Even though it took up only a tiny tail of the entire photoluminescence (P.L.) spectrum, especially beyond 1500 nm, the signals could still be well sensed by the InGaAs camera (**Supplementary Fig. 10**), which foreshadowed the great potential for NIR-IIb (beyond 1500 nm) fluorescence imaging.

The AIE dots suspended in phosphate buffer saline (PBS), serum, simulated intestinal fluid and gastric fluid were then exposed to continuous-wave (CW) 793 nm laser at a power density of 120 mW cm^{-2} for 30 min, whose power was higher than that during realistic imaging *in vivo*. As shown in **Supplementary Fig. 11**, the superior photostability and chemical stability in the extreme environments could be recognized. In addition, the toxicity and excretion of exogenous nanomaterials introduced into a body are of important concerns. With the AIE dots (2 mg kg^{-1}) intravenously injected into mice, NIR-II imaging beyond 1100 nm was accomplished to glean the emission from the whole bodies. Over a period of 4 h post injection, the signals in liver and intestines evidently accumulated, demonstrating the uptake from blood circulation (**Fig. 2e** & **Supplementary Fig. 12**). We collected the feces excreted from mice, recorded the fluorescence and observed the strong emission of the AIE dots. As shown in **Fig. 2e** and **Supplementary Fig. 12**, the excretion by the hepatobiliary pathway resulted in a dramatical intensity decrease of the signals in the organs within 44 days post injection, especially liver and intestines. The fluorescence intensity of the isolated liver and spleen after 6 weeks post-injection was also measured, which showed significant decrease (at least 98% and 97%, respectively) compared to that at 1st week post-injection (**Supplementary Fig. 13**). After 6 months post-injection, the biochemical test and blood routine test results showed that the dots did not influence on the hepatic and renal function, or peripheral blood cells (**Supplementary Tab. 1-4**). So far, no evidence showed obvious toxicity of the AIE dots *in vivo*, which could facilitate the pre-clinical trials in non-human primate.

High-spatial-resolution through-skull cerebrovascular microscopic imaging

In the fields of biological research, the deciphering of cerebrovasculature was inextricably linked to the exploration of neuroinformatics and brain-related theory in rodents, humans and other species[55]. Meanwhile, some common neurological disorders such as Alzheimer's or amyotrophic lateral sclerosis may result from dysfunction of cerebrovascular structure and/or function[56, 57]. In our study, AIE nanoparticles at such low doses (2 mg kg^{-1}) could render the cerebral vascular network under the cranial window of mice clearly visible (**Supplementary Fig. 14**). By axially tuning the relative position between the sample stage and the objective lens, the signals on each focal plane within nearly 870 μm below skull were almost thoroughly recorded and an ultra-high spatial resolution of merely ~2.4 μm was attained uncomplicatedly (**Supplementary**

Fig. 15).

The observation of brain vasculatures was then extended to non-human primates and we expanded on the feasibility of harmless AIE nanoparticles assisted NIR-II fluorescence imaging of the blood vascular structure in marmosets. NIR-II fluorescence wide-field microscopy is characterized as easy operation and minute loss of effective signals. In order to gather more NIR-II signals through the thinned skull, we collected fluorescence emission beyond 1100 nm in vessels. After intravenous injection of the AIE dots (20 mg kg^{-1}), a large view of cortical vasculature was preserved on the NIR-sensitive camera by a scan lens (LSM03). Tracking the periodic vibrations of the capillaries, we measured the respiratory rate and heart rate of the marmoset in time (**Fig. 3a-e**). The calculation well-echoed the actual values measured by an ECG (electrocardiogram) monitor (**Supplementary Fig. 16**). A typical micro cortical region was locked and the NIR-II through-skull tomographic angiography in brain was further conducted with a 25X objective. As we expected, imaging depth below skull reached nearly 700 μm eventually and a capillary of ~5.2 μm at ~200 μm was distinctly identified, which bettered previous records, owing to the extraordinarily bright AIE dots (**Fig. 3f-n**). After the nanoparticles were injected, the metabolites (feces and urine) of marmosets were collected at certain time points. All of the above operations involved the marmosets were performed in a sterile environment. We also focused on the excretion of nanoparticles from marmosets and the P.L. intensity of metabolites (feces and urine) was verified post-injection. As shown in **Fig. 3o**, the hepatobiliary excretion route in marmosets was confirmed, which was consistent with that in mice.

High-temporal-resolution through-skull cortical blood flow monitoring

The flow and circulation of blood maintain the normal operation of body. A stroke occurs when a cerebral cortical micro-vessel that delivers oxygen, nutrients and energy to the brain is either blocked by a clot or bursts[58]. An efficient method for real-time cerebrovascular monitoring means a great deal in the study of life sciences. In a fixed field of view, cortical vasculatures in marmosets with diverse functions always possess different rate and volume of blood flow. Assisted by the bright emission and biocompatibility of AIE dots, the adrift fluorescent micro-spots in blood could be readily captured by the microscope through the skull. We recorded the regions of interest continuously per 40 ms and the positions of the points as a function of time were plotted (**Fig. 4a, b and Supplementary Fig. 17**). Each blood capillary was repeatedly computed three times and averaged to obtain the mean flow rate of the six blood vessels in the selected area (**Fig. 4c**). Additionally, the type of blood vessels can be classified as veins based on the direction of flow, as veins collect blood from the branches, whereas arteries do the opposite

.

The aftermaths of a stroke primarily depend on the location of the obstruction and the extent of related brain tissue and it could lead to the alteration of blood flow

direction. NIR-II fluorescence wide-filed microscopic imaging could provide a noninvasive method for thrombosis monitoring. The diagnostics of cerebrovascular alteration after brain embolism with through-skull microscopy was further explored. A CW 532 nm laser beam was selected as the excitation source and introduced into the wide-field microscopy. After collimated, reflected and reduced, it eventually irradiated evenly the sample with tiny area. The schematic illustration for induction of photothrombotic stroke under excitation of 532 nm CW laser was shown in **Fig. 4d**. After intravenously injected into mice (20 mg kg^{-1}), the photosensitizer (Rose Bengal) could release singlet oxygen ($^1O_2$) under excitation that then adhered to and destroyed the endothelial cells of blood vessels. Platelets that spontaneously stuck together in damaged regions could then form clots, which would eventually yield cerebral strokes.

The photothrombotic induction of capillary ischemia was observed firstly in mice with cranial windows. **Supplementary Fig. 18a** showed a large-field cerebrovascular image post-injection of AIE dots, in which a region of ~454 μm × ~363 μm containing two characteristic capillaries was selected (**Supplementary Fig. 18b**). After the Rose Bengal injected into the mouse, the area outlined by the green dashed line was continuously illuminated for 150 seconds by 532 nm laser (~20 mW before the objective). **Supplementary Fig. 18c** revealed that the stockpiled platelets impeded the blood flow, giving the dots unable for continuous circulation. Before long the slight obstruction was flushed away by the high-speed blood that contained AIE dots and the two once-occluded capillaries returned to normal in ~230 s (**Supplementary Fig. 18c-e**). Judging from the blood flow direction, these two vessels could be recognized as veins. Next, we shrank the irradiation area to increase energy density in another mouse. After irradiation for 150 s, there was no obvious recovery in the next 60 min, while some vascular hyperplasia could be nevertheless observed (**Supplementary Fig. 19**). Moreover, the photothrombotic thrombosis showed multiple effects on nearby blood vessels, including vasoconstriction, vasodilation, hyperplasia, et.al, as shown in **Supplementary Fig. 20**.

Real-time through-skull functional imaging in brain assisted by the AIE dots was further conducted on non-human primates and cerebrovascular alteration after brain embolism was observed on marmosets, giving another noninvasive diagnostics modality for primates. Thanks mainly to the ultrahigh-brightness of the AIE dots, the blockage of cortical vasculatures below the skull was exceedingly visible post irradiation of the CW 532 nm laser for 3 min (**Fig. 5e-h**). Interestingly, the real-time video of the ROI wrote down the blood flow arrest or even reflux in other side branches

NIR-IIb fluorescence high-spatial-frequency noninvasive gastrointestinal imaging

Pathologies of GI tract such as neoplastic and functional pathologies, chronic inflammatory diseases, and nontraumatic emergency causing occlusion are multifarious and patients of diverse ages can be affected by such diseases. Consequently, clinically common diagnostic approaches, like computerized tomography (CT) or magnetic

resonance imaging (MRI), should be reassessed seriously in view of the ionizing radiation, limited spatial resolution or time consuming[59]. NIR-IIb (1500-1700 nm) fluorescence imaging with the extremely low-scattering overcomes the above shortcomings to a certain degree and stands out in optical biological imaging on account of its superlative penetration depth in complex refractive index media. Thus, it is of great clinical value in functional diagnosis of the GI tract. The process of the dots entering the colon from the ileum is recorded.

As a suitable contrast agent, the AIE dots in our work was demonstrated possessing excellent stability and strong NIR-IIb emission. After intragastric administration (15 mg kg^{-1}), the NIR-IIb fluorescence GI imaging was carried out in mice. During the first 20 minutes, the fluorescent probe passed into the jejunum from the duodenum and the ileum was lighted up progressively within 1 h post-treatment (**Supplementary Fig. 21**). The excretion from ileum to colon was also recorded throughout the next 9 h. The typical image at 22 h precisely showed the feces that have not yet been excreted thoroughly. In contrast to the increasingly blurry details imaged in the NIR-II region beyond 1400 nm, 1300 nm, 1200 nm, 1100 nm, 1000 nm, and 900 nm (**Supplementary Fig. 22**), we could see that much sharper images were got by extending the wavelength of the detected photons and the sharpest resolution and highest signal-to-background ratio (the background was defined as the valley between the two peaks.) images of ileum were obtained beyond 1500 nm. After 32 h, the feces almost gathered all the fluorescent emission. Importantly, the main organs remained no fluorescent signals at all at 3 d post-treatment and the safety of the AIE dots was demonstrated (**Supplementary Fig. 23**).

Next, we evaluated NIR-IIb GI imaging in non-human primates, which might contribute to the clinical applications in the future. The operation illustration was shown in **Fig. 5a** and the sharp NIR-IIb images of marmosets deciphered the complicated bowel structure well (**Fig. 5b-m** & **Supplementary Fig. 24**) post feeding (15 mg kg^{-1}). At 60 min, we analyzed the small intestine structure in the traditional NIR-II (beyond 1000 nm), the NIR-IIa (beyond 1300 nm), and the NIR-IIb (beyond 1500 nm). As shown in **Fig. 5j**, the gap between intestines was accurately identified as 1.04 mm without being submerged in fluorescence, benefiting from the sharp edges in the NIR-IIb image and the stable bright emission of the probe. To further figure out the superiority of NIR-IIb fluorescence imaging, we singled out the representative parts separately from the images beyond 1000 nm, 1300 nm, and 1500 nm and their spectrum maps were shown in **Fig. 5h-j** by fast Fourier transformation (FFT) (**Supplementary Fig. 25**). The fact that the NIR-IIb image is in possession of the most abundant high-frequency information was confirmed, that is to say, the imaging technology beyond 1500 nm possesses precise expression of details and edges. As expected, the AIE dots were also excreted smoothly from the marmosets eventually (**Fig. 5n**). This work is the first attempt to apply NIR-IIb fluorescence imaging technology in primate mammals, and we believe it holds immeasurable significance.

Outlook

Aggregation-induced emission has been respected as a major research focus, since the uncommon emission behaviors were revealed around two decades ago[5, 60]. To date, the utilization of AIE materials in a wide variety of high-tech areas have triggered much widespread concern[61]. Low toxicity and good biocompatibility equipped these organic fluorophores with huge potential for biological applications[62, 63]. Besides, intermolecular interactions strongly heightened the emission efficiency of some special luminophores, and thus some deep-red and even near-infrared strong emitters were designed[20, 27, 64]. On the other hand, NIR-II fluorescence is known for its suppressed low tissue-scattering and deep biological penetration and has attracted much scientific attention in recent years[65, 66]. In view of the low luminous efficiency of traditional near-infrared fluorescent probes, the exploration of AIE has undoubtedly boosted the further development of NIR-II fluorescence imaging.

It is critical to extend the AIE dots assisted fluorescence imaging to non-human primates for the further clinical application. Despite a series of reported NIR-II fluorophores showed nearly nontoxicity *in vitro* or *in vivo* and even good renal or biliary excretion in rodents[45, 52, 67], to date, there has been no evidence about the excretion in non-human primates which are often considered the ultimate translational research model due to their close homology to human being. In current work, the AIE nanoparticles after PEGylation were proved undetectably bio-toxic and well biocompatible. Almost all the intravenously administrated AIE dots were excreted from mice in 44 days and the main organs showed no residual fluorescence within xxx days. Not only that, the strong emission of marmoset dejecta also testified the obvious hepatobiliary excretion within 26 days post intravenous injection. Hence, on the strength of NIR-II fluorescence imaging technology, low biological risk of the AIE dots could be validated and it is therefore potentially possible to apply the fluorophores to preclinical or even clinical research.

Operational safety often takes priority in surgery and craniotomy always assumes a great risk. Noninvasive through-skull cerebrovascular microscopic observation was conducted with high spatial and temporal resolution in non-human primates, relying on the ultrabright AIE dots. Capillaries of a few microns (eg. ~5.2 μm) or the vessels at micrometer-deep position (eg. ~0.7 mm) could be clearly distinguished below skull. Speedy recorded images frame by frame could well track the blood flow whose mean value was calculated as millimetric scale per second. So far, there have existed no other fluorescent probes successfully utilized for through-skull cortical vasculature fluorescence imaging in non-human primates. We believe such high-precision analysis of capillaries would contribute to the study of angiogenesis, neurodevelopment, as well as the differentiation of glial cells owing to the tightly association among them, which would possibly provide new thoughts for brain function development research.

The NIR-IIb window has proved ideal for optical imaging in biological media with complex refractive index, such as mammals[52, 53, 64]. However, a scarcity of efficient probes with long emission wavelength impede the next step yet. It is encouraging that the AIE dots we reported exhibited extremely bright fluorescence even beyond 1500 nm, bringing us a versatile NIR-IIb dye capable of ultrahigh-definition GI imaging in non-human primates. In contrast of NIR-II (beyond 1000 nm) and NIR-IIa (beyond 1300

nm) images, the NIR-IIb image stored the most abundant high-frequency components, which reaffirmed its direct visualization of details. The clear depiction of complicated intestinal structure in marmosets undoubtedly contributes to improving the accuracy of early diagnosis of GI disorders, and promotes the clinical imaging development in the near future.

Non-human primates are acknowledged as subjects in studies involving toxicology, reproductive biology, neurology, behavior, cognition, and more, thus always taking huge responsibility for human medical research. We took the lead to apply biocompatible AIE dots to non-human primates fluorescence imaging and splendidly performed through-skull cortical vasculature imaging and NIR-IIb fluorescence GI imaging in non-human primates for the first time. Future research will focus on the exhaustive toxicity investigation of the AIE nanoparticles on primates. We wish that the work could promote the development of AIE in large animal application and further clinical translation can be inspired through our efforts.

Methods

Synthesis

For all synthesis details, please see the Supplementary Information.

PEGylation of AIE dots

1 mL of tetrahydrofuran (THF) solution containing 2 mg of OTPA-BBT AIEgen, and 10 mg of pluronic F-127 was poured into 10 mL of deionized water. Followed by sonication with a microtip probe sonicator (XL2000, Misonix Incorporated, NY) for 2 min. The residue THF solvent was evaporated by violent stirring the suspension in fume hood overnight, and colloidal solution was obtained and used directly. AIE dots were subjected to ultrafiltration for further purification.

Animal handing

All experimental procedures were approved by Animal Use and Care Committee at Zhejiang University following the NIH guidelines. Experimental animals: Mice (BALB/c and nude mice) and common marmosets (Callithrix jacchus). We used young marmosets (150-200 g), 6~7 months of age, with either sex in this study. BALB/c and nude mice were fed with water and food with a normal 12 h light/dark cycle, and the surrounding relative humidity level was 55–65% and the temperature was ~25 °C. Marmosets are generally raised in a suitable environment of about 26 ℃, the indoor temperature was kept constant, and the relative humidity was around 40% ~ 70%. All groups within study contained n = 10 mice and n = 4 monkeys.

Surgery for cerebrovascular microscopic imaging

Marmosets (Callithrix jacchus,150 g-200 g) were initially anesthetized with ketamine (30 mg $kgbw^{-1}$) by intramuscular injection and maintained with 0.5–3.0% isoflurane in 100% medical oxygen by a facemask connect to an inhalation anesthesia machine (RWD 510). The animals were placed in a marmoset stereotaxic frame (SR-

5C-HT, Narishige) and the body temperature was maintained by a thermostatic heating pad at 37°C. The heart rates (180–300 bpm) and respiration rates (25–40 breaths per minute) were monitored and arterial oxygen saturation (SpO_2) was kept above 95% (v/v) by adjusting the concentration of isoflurane. The head of the animal was shaved with small-animal hair clippers and scrubbed with three washes of 10% (v/v) povidone iodine, followed by 70% (v/v) ethanol. All additional surgical steps were conducted under aseptic or sterile conditions. A midline incision was made to expose the skull. A craniotomy with 5.0 mm in diameter was grinded through ~50% of the thickness of the bone in a target imaging site using a mini handheld cranial drill (RWD 78001). A round glass coverslip was placed on the top of the craniotomy and secured by cyanoacrylate adhesive and dental cement, respectively, to create an observing window for the cerebral vessels imaging later. A wall was built surrounded the glass coverslip with dental cement to hold deuterium oxide linking the cranial window and objective. The unnecessary glue covering the coverslip was carefully removed by using blunt side of scalpel under an operating microscope. After the imaging sessions were finished, the coverslip was removed from the skull and the wounds were flushed with fresh saline. Finally, sterilized sutures were tied to repairing a large surgical defect on the scalp along the midline of the skull. Animals were administrated with ceftriaxone (22 mg $kgbw^{-1}$) for the subsequent 7 days to minimize inflammation and infection.

Procedures for cerebrovascular microscopic imaging

After anaesthesia, the marmosets were immobilized on a two-dimensional (2D) translational stage with adjustable X and Y axis, placing the region of interest right under the objective lens. Then 10 cc warm glucose in normal saline and AIE dots (2 mg kg^{-1}) were administrated by intravenous catheter, respectively. As shown in **Supplementary Fig. 26**, a collimated CW 793 nm laser was introduced into the modified epi-illumination (RX50, Sunny, China), expanded by lens, reflexed by a long-pass dichroic mirror and focused on the back focal plane of the objective lens, eventually irradiating the sample evenly and securely. The excitation light from the objective lens penetrated the skull and meninges to light up the dots in the blood vessels. In turn, the emission signals beyond 1100 nm were collected by the objective lens through the skull and the dichroic mirror, and afterwards focused on an NIR-sensitive camera (SW640, Tekwin, China). To purify the NIR-II signals, the long-pass optical filter was set in front of the 2D-detector. During imaging, the images at increasing depths were recorded by vertically tuning the epi-illumination. Another laser beam of 532 nm was selected for the photothrombotic induction. Contrary to the mention above, the excitation light was focused in the brain by the objective for a local photodynamic damage. Thrombus was induced and monitored by switching the excitation source and equipped optical set-up.

Collocation and detection of metabolites

During the cerebrovascular microscopic imaging session, we administrated AIE dots onto animals' bodies via intravenous catheter for the experimental group and saline for control group. Both groups were raised in the same environments. We collected the

urine and feces from both groups one certain day per week for 6-8 weeks. In the GI imaging experiment, we collected feces and urine right after the animals was fed with fluorescent particles. The collection was lasted for 3-5 days in the experimental animals, while collecting excretion from the animals in the control group fed with saline, and there should be no contact between urine and feces during collection.

Procedures for gastrointestinal imaging

Marmosets were trained to be fed by syringe without wasting food for 3-5 days before GI imaging experiment. During the imaging sessions, animal was fed with AIE dots (15 mg kg^{-1}) by syringe. The animal was anesthetized with ketamine (30 mg $kgbw^{-1}$) by intramuscular injection and placed on a height-adjustable table with belly up after the hair on the bell was shaved. As shown in **Supplementary Fig. 27**, the expanded laser (793 nm, 120 mW cm^{-2}) illuminated the whole belly and a fixed focus lens (TKL35, Tekwin, China) collected the emission signals from GI tract. The belly of the animal was imaged for 30s every 5 minutes in the first thirty minutes and every 2 hours in the following time of the experiments. While the animal was in awake state, we hold the animal still with belly up for 30s for imaging by leather gloves. The animal was allowed to return back to the home cage for eating and drinking in the imaging interval of the experiments. After GI imaging experiment was finished, the experimental animals were raised in single cage for 3-5 days, which is convenient for collecting the urine and feces.

Image signal was processed by 2-D Fourier transform

Low-frequency components in the spectrum correspond to areas with flat gray scale variations in the time-domain image where energy is mainly concentrated, while high-frequency components correspond to areas with sharp grayscale variations, which are principally represented by edges and details in the original image.

After an image undergoes DFT, the low-frequency components are reflected in the four corner parts of spectrum. To facilitate the observation of the spectrum distribution, the low-frequency components are shifted to the spectrum center through the spectrum centralization (**Supplementary Fig. 25**) and the outer part of spectrum is basically the high frequency component. As shown in **Fig. 5d-f**, the more high-frequency information an image contains, the more detail and clarity it contains.

Acknowledgements

This work was supported by National Natural Science Foundation of China (61735016, 61975172, 61703365, 31871056, 91732302 and 21788102), Zhejiang Provincial Natural Science Foundation of China (LR17F050001), the National Key Research and Development Program of China (2018YFC1005003 and 2018YFE0190200), Fundamental Research Funds for the Central Universities (2018QN81008), Research Grants Council of Hong Kong (C6009-17G and A-HKUST605/16) and Innovation and Technology Commission (ITC-CNERC14SC01 and ITCPD/17-9).

Author contributions

J.Q. (J. Qian), L.G. and T.B.Z. conceived the whole project. J.Q. (J. Qian) and Z.F. designed the study and drafted the manuscript. Z.F., S.B. and J.Q. (J. Qi) completed all the experiments. Y.Z. and X.Y. took part in the animal experiments and helped with data processing. H.N. and M.H. contributed to the optical measurement. D.W. checked the manuscript. D.W., X.F. and D.X. mainly conducted the biomedical analysis. J.G. and P.W. contributed to synthesis of the molecule. X.L. and J.W.Y.L. joined the discussion. X.L. performed the complex surgery.

Competing interests

The authors declare no competing financial interests.

References

1. Chan J, Dodani SC, Chang CJ. Reaction-based small-molecule fluorescent probes for chemoselective bioimaging. *Nat Chem* 2012, **4**(12)**:** 973-984.
2. Pan Y, Volkmer JP, Mach KE, Rouse RV, Liu JJ, Sahoo D*, et al.* Endoscopic molecular imaging of human bladder cancer using a CD47 antibody. *Sci Transl Med* 2014, **6**(260).
3. Vahrmeijer AL, Hutteman M, van der Vorst JR, van de Velde CJH, Frangioni JV. Image-guided cancer surgery using near-infrared fluorescence. *Nat Rev Clin Oncol* 2013, **10**(9)**:** 507-518.
4. Birks JB. Photophysics of Aromatic Molecules. *John Wiley and Sons Ltd* 1970**:** 403-489.
5. Luo JD, Xie ZL, Lam JWY, Cheng L, Chen HY, Qiu CF*, et al.* Aggregation-induced emission of 1-methyl-1,2,3,4,5-pentaphenylsilole. *Chem Commun* 2001(18)**:** 1740-1741.
6. Li CY, Luo XL, Zhao WJ, Li CH, Liu ZP, Bo ZS*, et al.* Switching the emission of tetrakis(4-methoxyphenyl)ethylene among three colors in the solid state. *New J Chem* 2013, **37**(6)**:** 1696-1699.
7. Song N, Chen DX, Qiu YC, Yang XY, Xu B, Tian W*, et al.* Stimuli-responsive blue fluorescent supramolecular polymers based on a pillar[5]arene tetramer. *Chem Commun* 2014, **50**(60)**:** 8231-8234.
8. Peterson JJ, Davis AR, Werre M, Coughlin EB, Carter KR. Carborane-Containing Poly(fluorene): Response to Solvent Vapors and Amines. *Acs Appl Mater Inter* 2011, **3**(6)**:** 1796-1799.
9. Ma CP, Xu BJ, Xie GY, He JJ, Zhou X, Peng BY*, et al.* An AIE-active luminophore with tunable and remarkable fluorescence switching based on the piezo and protonation-deprotonation control. *Chem Commun* 2014, **50**(55)**:** 7374-7377.
10. Huang J, Tang RL, Zhang T, Li QQ, Yu G, Xie SY*, et al.* A New Approach to Prepare Efficient Blue AIE Emitters for Undoped OLEDs. *Chem-Eur J* 2014,

20(18)**:** 5317-5326.
11. Zhao N, Zhang C, Lam JWY, Zhao YS, Tang BZ. An Aggregation-Induced Emission Luminogen with Efficient Luminescent Mechanochromism and Optical Waveguiding Properties. *Asian J Org Chem* 2014, **3**(2)**:** 118-121.
12. Yuan XP, Zhao M, Guo XJ, Li Y, Yu Y, Gan ZS*, et al.* Ultra-high capacity for three-dimensional optical data storage inside transparent fluorescent tape. *Opt Lett* 2020, **45**(6)**:** 1535-1538.
13. Wang XR, Hu JM, Zhang GY, Liu SY. Highly Selective Fluorogenic Multianalyte Biosensors Constructed via Enzyme-Catalyzed Coupling and Aggregation-Induced Emission. *J Am Chem Soc* 2014, **136**(28)**:** 9890-9893.
14. Liu Y, Deng CM, Tang L, Qin AJ, Hu RR, Sun JZ*, et al.* Specific Detection of D-Glucose by a Tetraphenylethene-Based Fluorescent Sensor. *J Am Chem Soc* 2011, **133**(4)**:** 660-663.
15. Mei J, Wang YJ, Tong JQ, Wang J, Qin AJ, Sun JZ*, et al.* Discriminatory Detection of Cysteine and Homocysteine Based on Dialdehyde-Functionalized Aggregation-Induced Emission Fluorophores. *Chem-Eur J* 2013, **19**(2)**:** 612-619.
16. Qian J, Tang BZ. AIE Luminogens for Bioimaging and Theranostics: from Organelles to Animals. *Chem-Us* 2017, **3**(1)**:** 56-91.
17. Zhang RY, Duan YK, Liu B. Recent advances of AIE dots in NIR imaging and phototherapy. *Nanoscale* 2019, **11**(41)**:** 19241-19250.
18. Ding D, Li K, Liu B, Tang BZ. Bioprobes Based on AIE Fluorogens. *Accounts Chem Res* 2013, **46**(11)**:** 2441-2453.
19. Kwok RTK, Leung CWT, Lam JWY, Tang BZ. Biosensing by luminogens with aggregation-induced emission characteristics. *Chem Soc Rev* 2015, **44**(13)**:** 4228-4238.
20. Qi J, Sun CW, Zebibula A, Zhang HQ, Kwok RTK, Zhao XY*, et al.* Real-Time and High-Resolution Bioimaging with Bright Aggregation-Induced Emission Dots in Short-Wave Infrared Region. *Adv Mater* 2018, **30**(12).
21. Alifu N, Zebibula A, Qi J, Zhang HQ, Sun CW, Yu XM*, et al.* Single-Molecular Near-Infrared-II Theranostic Systems: Ultrastable Aggregation-Induced Emission Nanoparticles for Long-Term Tracing and Efficient Photothermal Therapy. *Acs Nano* 2018, **12**(11)**:** 11282-11293.
22. Yu WB, Guo B, Zhang HQ, Zhou J, Yu XM, Zhu L*, et al.* NIR-II fluorescence in vivo confocal microscopy with aggregation-induced emission dots. *Sci Bull* 2019, **64**(6)**:** 410-416.
23. Sheng ZH, Guo B, Hu DH, Xu SD, Wu WB, Liew WH*, et al.* Bright Aggregation-Induced-Emission Dots for Targeted Synergetic NIR-II Fluorescence and NIR-I Photoacoustic Imaging of Orthotopic Brain Tumors. *Adv Mater* 2018, **30**(29).
24. Lin JC, Zeng XD, Xiao YL, Tang L, Nong JX, Liu YF*, et al.* Novel near-infrared II aggregation-induced emission dots for in vivo bioimaging. *Chem Sci* 2019, **10**(4)**:** 1219-1226.
25. Wu W, Yang YQ, Yang Y, Yang YM, Zhang KY, Guo L*, et al.* Molecular

Engineering of an Organic NIR-II Fluorophore with Aggregation-Induced Emission Characteristics for In Vivo Imaging. *Small* 2019, **15**(20).

26. Liu SJ, Chen C, Li YY, Zhang HK, Liu JK, Wang R*, et al.* Constitutional Isomerization Enables Bright NIR-II AIEgen for Brain-Inflammation Imaging. *Adv Funct Mater* 2019.
27. Xu PF, Kang F, Yang WD, Zhang MR, Dang RL, Jiang P*, et al.* Molecular engineering of a high quantum yield NIR-II molecular fluorophore with aggregation-induced emission (AIE) characteristics for in vivo imaging. *Nanoscale* 2020, **12**(8)**:** 5084-5090.
28. Gao S, Wei GG, Zhang SH, Zheng BB, Xu JJ, Chen GX*, et al.* Albumin tailoring fluorescence and photothermal conversion effect of near-infrared-II fluorophore with aggregation-induced emission characteristics. *Nat Commun* 2019, **10**.
29. Zhang Z, Fang XF, Liu ZH, Liu HC, Chen DD, He SQ*, et al.* Semiconducting Polymer Dots with Dual-Enhanced NIR-IIa Fluorescence for Through-Skull Mouse-Brain Imaging. *Angew Chem Int Edit* 2020, **59**(9)**:** 3691-3698.
30. Homman-Ludiye J, Bourne JA. The marmoset: An emerging model to unravel the evolution and development of the primate neocortex. *Developmental Neurobiology* 2017, **77**(3)**:** 263-272.
31. Saito A. The marmoset as a model for the study of primate parental behavior. *Neurosci Res* 2015, **93:** 99-109.
32. Ghahremani M, Hutchison RM, Menon RS, Everling S. Frontoparietal Functional Connectivity in the Common Marmoset. *Cerebral Cortex* 2017, **27**(8)**:** 3890-3905.
33. Mansfield K. Marmoset models commonly used in biomedical research. *Comparative Medicine* 2003, **53**(4)**:** 383-392.
34. Bert A, Abbott DH, Nakamura K, Fuchs E. The marmoset monkey: a multi-purpose preclinical and translational model of human biology and disease. *Drug Discovery Today* 2012, **17**(21-22)**:** 1160-1165.
35. Reemst K, Noctor SC, Lucassen PJ, Hol EM. The Indispensable Roles of Microglia and Astrocytes during Brain Development. *Frontiers in Human Neuroscience* 2016, **10**.
36. Fonta C, Imbert M. Vascularization in the primate visual cortex during development. *Cerebral Cortex* 2002, **12**(2)**:** 199-211.
37. Zheng D, Lamantia AS, Purves D. SPECIALIZED VASCULARIZATION OF THE PRIMATE VISUAL-CORTEX. *Journal of Neuroscience* 1991, **11**(8)**:** 2622-2629.
38. Harel N, Bolan PJ, Turner R, Ugurbil K, Yacoub E. Recent Advances in High-Resolution MR Application and Its Implications for Neurovascular Coupling Research. *Frontiers in neuroenergetics* 2010, **2:** 130.
39. Casteleyn C, Bakker J. Chapter 2 - The Anatomy of the Common Marmoset. In: Marini R, Wachtman L, Tardif S, Mansfield K, Fox J (eds). *The Common Marmoset in Captivity and Biomedical Research*. Academic Press, 2019, pp 17-41.
40. Kong F, Singh RP. Disintegration of solid foods in human stomach. *J Food Sci*

2008, **73**(5)**:** R67-R80.
41. Adams JY, Johnson M, Sato M, Berger F, Gambhir SS, Carey M*, et al.* Visualization of advanced human prostate cancer lesions in living mice by a targeted gene transfer vector and optical imaging. *Nat Med* 2002, **8**(8)**:** 891-896.
42. Choi HS, Gibbs SL, Lee JH, Kim SH, Ashitate Y, Liu FB*, et al.* Targeted zwitterionic near-infrared fluorophores for improved optical imaging. *Nat Biotechnol* 2013, **31**(2)**:** 148-153.
43. Zhang RR, Schroeder AB, Grudzinski JJ, Rosenthal EL, Warram JM, Pinchuk AN*, et al.* Beyond the margins: real-time detection of cancer using targeted fluorophores. *Nat Rev Clin Oncol* 2017, **14**(6)**:** 347-364.
44. Hong GS, Lee JC, Robinson JT, Raaz U, Xie LM, Huang NF*, et al.* Multifunctional in vivo vascular imaging using near-infrared II fluorescence. *Nat Med* 2012, **18**(12)**:** 1841-1846.
45. Hong GS, Robinson JT, Zhang YJ, Diao S, Antaris AL, Wang QB*, et al.* In Vivo Fluorescence Imaging with Ag2S Quantum Dots in the Second Near-Infrared Region. *Angew Chem Int Edit* 2012, **51**(39)**:** 9818-9821.
46. Zebibula A, Alifu N, Xia LQ, Sun CW, Yu XM, Xue DW*, et al.* Ultrastable and Biocompatible NIR-II Quantum Dots for Functional Bioimaging. *Adv Funct Mater* 2018, **28**(9).
47. Guo B, Feng Z, Hu DH, Xu SD, Middha E, Pan YT*, et al.* Precise Deciphering of Brain Vasculatures and Microscopic Tumors with Dual NIR-II Fluorescence and Photoacoustic Imaging. *Adv Mater* 2019, **31**(30).
48. Feng Z, Yu XM, Jiang MX, Zhu L, Zhang Y, Yang W*, et al.* Excretable IR-820 for in vivo NIR-II fluorescence cerebrovascular imaging and photothermal therapy of subcutaneous tumor. *Theranostics* 2019, **9**(19)**:** 5706-5719.
49. Yu XM, Feng Z, Cai ZC, Jiang MX, Xue DW, Zhu L*, et al.* Deciphering of cerebrovasculatures via ICG-assisted NIR-II fluorescence microscopy. *J Mater Chem B* 2019, **7**(42)**:** 6623-6629.
50. Wu D, Xue DW, Zhou J, Wang YF, Feng Z, Xu JJ*, et al.* Extrahepatic cholangiography in near-infrared II window with the clinically approved fluorescence agent indocyanine green: a promising imaging technology for intraoperative diagnosis. *Theranostics* 2020, **10**(8)**:** 3636-3651.
51. Diao S, Blackburn JL, Hong GS, Antaris AL, Chang JL, Wu JZ*, et al.* Fluorescence Imaging In Vivo at Wavelengths beyond 1500 nm. *Angew Chem Int Edit* 2015, **54**(49)**:** 14758-14762.
52. Zhang MX, Yue JY, Cui R, Ma ZR, Wan H, Wang FF*, et al.* Bright quantum dots emitting at similar to 1,600 nm in the NIR-IIb window for deep tissue fluorescence imaging. *P Natl Acad Sci USA* 2018, **115**(26)**:** 6590-6595.
53. Zhong YT, Ma ZR, Wang FF, Wang X, Yang YJ, Liu YL*, et al.* In vivo molecular imaging for immunotherapy using ultra-bright near-infrared-IIb rare-earth nanoparticles. *Nat Biotechnol* 2019, **37**(11)**:** 1322-1331.
54. Cai ZC, Zhu L, Wang MQ, Roe AW, Xi W, Qian J. NIR-II fluorescence microscopic imaging of cortical vasculature in non-human primates. *Theranostics* 2020, **10**(9)**:** 4265-4276.

55. Storkebaum E, Quaegebeur A, Vikkula M, Carmeliet P. Cerebrovascular disorders: molecular insights and therapeutic opportunities. *Nature neuroscience* 2011, **14**(11)**:** 1390-1397.
56. Kelleher RJ, Soiza RL. Evidence of endothelial dysfunction in the development of Alzheimer's disease: Is Alzheimer's a vascular disorder? *American journal of cardiovascular disease* 2013, **3**(4)**:** 197-226.
57. Sweeney MD, Kisler K, Montagne A, Toga AW, Zlokovic BV. The role of brain vasculature in neurodegenerative disorders. *Nature neuroscience* 2018, **21**(10)**:** 1318-1331.
58. Sierra C, Coca A, Schiffrin EL. Vascular mechanisms in the pathogenesis of stroke. *Current hypertension reports* 2011, **13**(3)**:** 200-207.
59. Siebert E, Bohner G, Dewey M, Masuhr F, Hoffmann KT, Mews J*, et al.* 320-slice CT neuroimaging: initial clinical experience and image quality evaluation. *The British journal of radiology* 2009, **82**(979)**:** 561-570.
60. Hong YN, Lam JWY, Tang BZ. Aggregation-induced emission. *Chem Soc Rev* 2011, **40**(11)**:** 5361-5388.
61. Mei J, Leung NLC, Kwok RTK, Lam JWY, Tang BZ. Aggregation-Induced Emission: Together We Shine, United We Soar! *Chem Rev* 2015, **115**(21)**:** 11718-11940.
62. Cai XL, Liu B. Aggregation-Induced Emission: Recent Advances in Materials and Biomedical Applications. *Angew Chem Int Edit* 2020.
63. Hu F, Xu SD, Liu B. Photosensitizers with Aggregation-Induced Emission: Materials and Biomedical Applications. *Adv Mater* 2018, **30**(45).
64. Li YY, Cai ZC, Liu SJ, Zhang HK, Wong STH, Lam JWY*, et al.* Design of AIEgens for near-infrared IIb imaging through structural modulation at molecular and morphological levels. *Nat Commun* 2020, **11**(1)**:** 1255.
65. Hong GS, Diao S, Chang JL, Antaris AL, Chen CX, Zhang B*, et al.* Through-skull fluorescence imaging of the brain in a new near-infrared window. *Nat Photonics* 2014, **8**(9)**:** 723-730.
66. Yang YQ, Fan XX, Li L, Yang YM, Nuernisha A, Xue DW*, et al.* Semiconducting Polymer Nanoparticles as Theranostic System for Near-Infrared-II Fluorescence Imaging and Photothermal Therapy under Safe Laser Fluence. *Acs Nano* 2020, **14**(2)**:** 2509-2521.
67. Antaris AL, Chen H, Cheng K, Sun Y, Hong GS, Qu CR*, et al.* A small-molecule dye for NIR-II imaging. *Nat Mater* 2016, **15**(2)**:** 235-242.

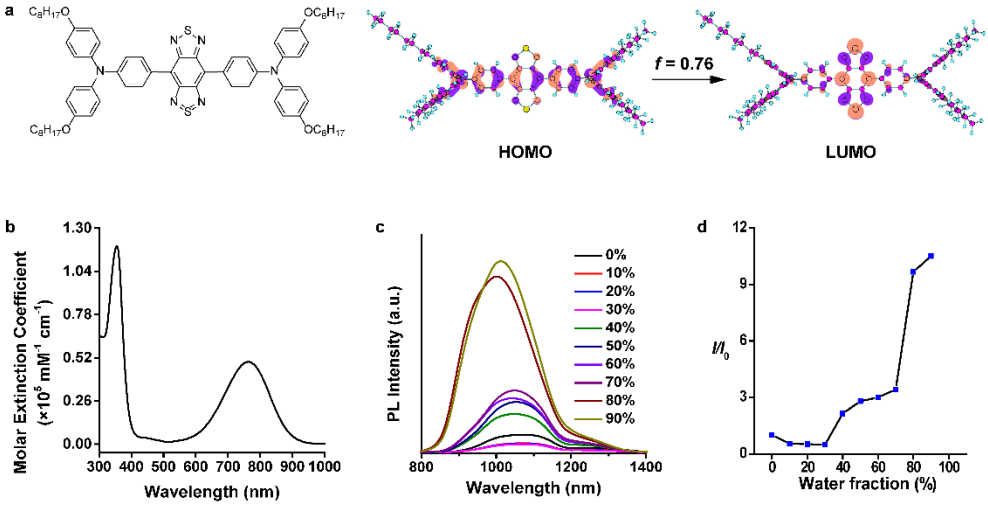

Fig. 1 | (a) The molecular structure. (b) The molar extinction coefficient of the OTPA-BBT. (c) PL spectra of OTPA-BBT in THF/H_2O mixtures with different water fractions (f_w). (d) Plot of PL peak intensity of compound OTPA-BBT versus water fraction (f_w) of THF/water mixture. I_0 and I are the PL peak intensities of the OTPA-BBT in pure THF (f_w = 0) and THF/water mixtures with specific f_ws, respectively.

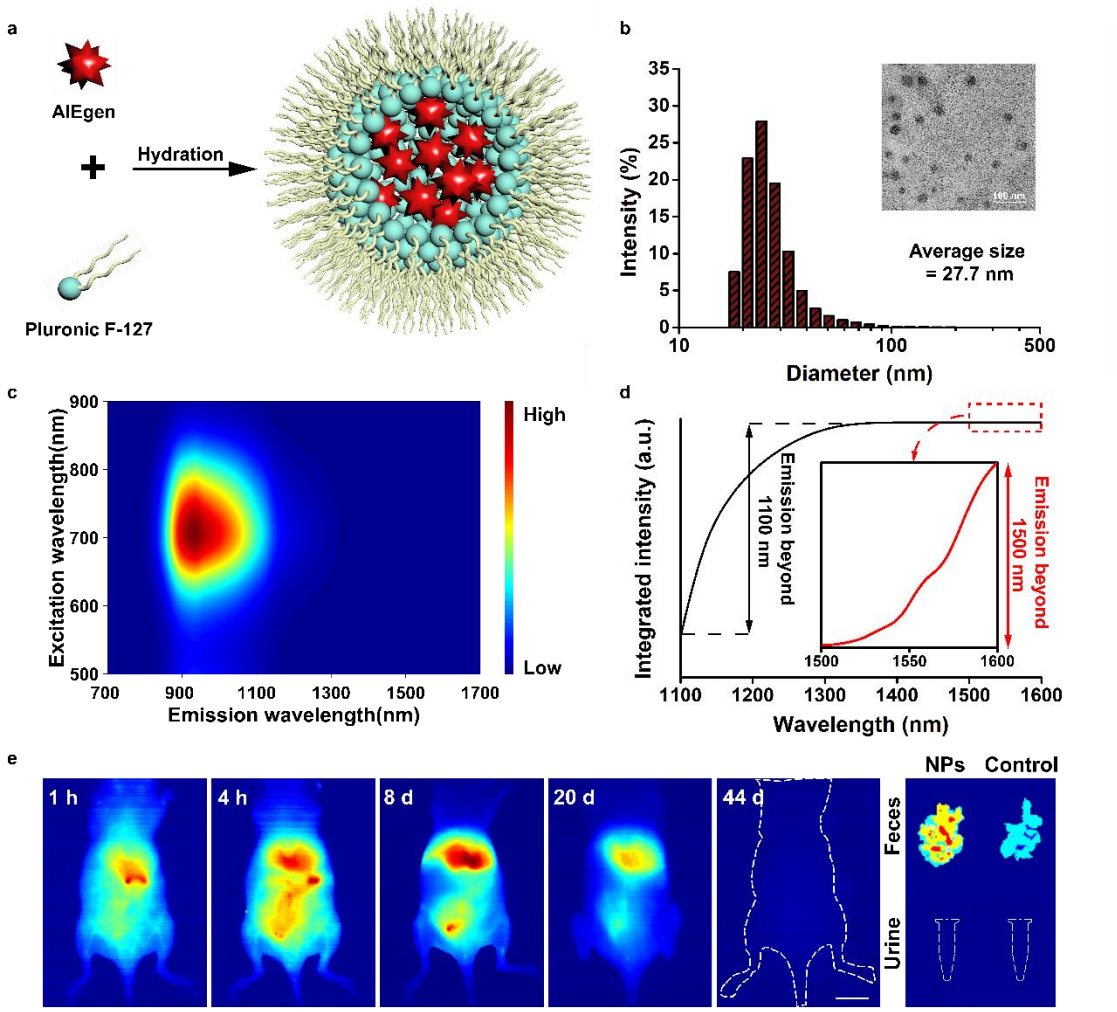

Fig. 2 | (a) Schematic illustration of the fabrication of AIE dots. **(b)** Representative DLS result and TEM image of the AIE dots. **(c)** PL excitation mapping of AIE dots in aqueous dispersion. **(d)** The integration of the fluorescence intensity. The difference on the ordinate represents the total fluorescence intensity in a certain wavelength. The insert image showed the NIR-IIb emission. **(e)** The excretion monitoring of mice post intravenous injection (2 mg kg^{-1}).

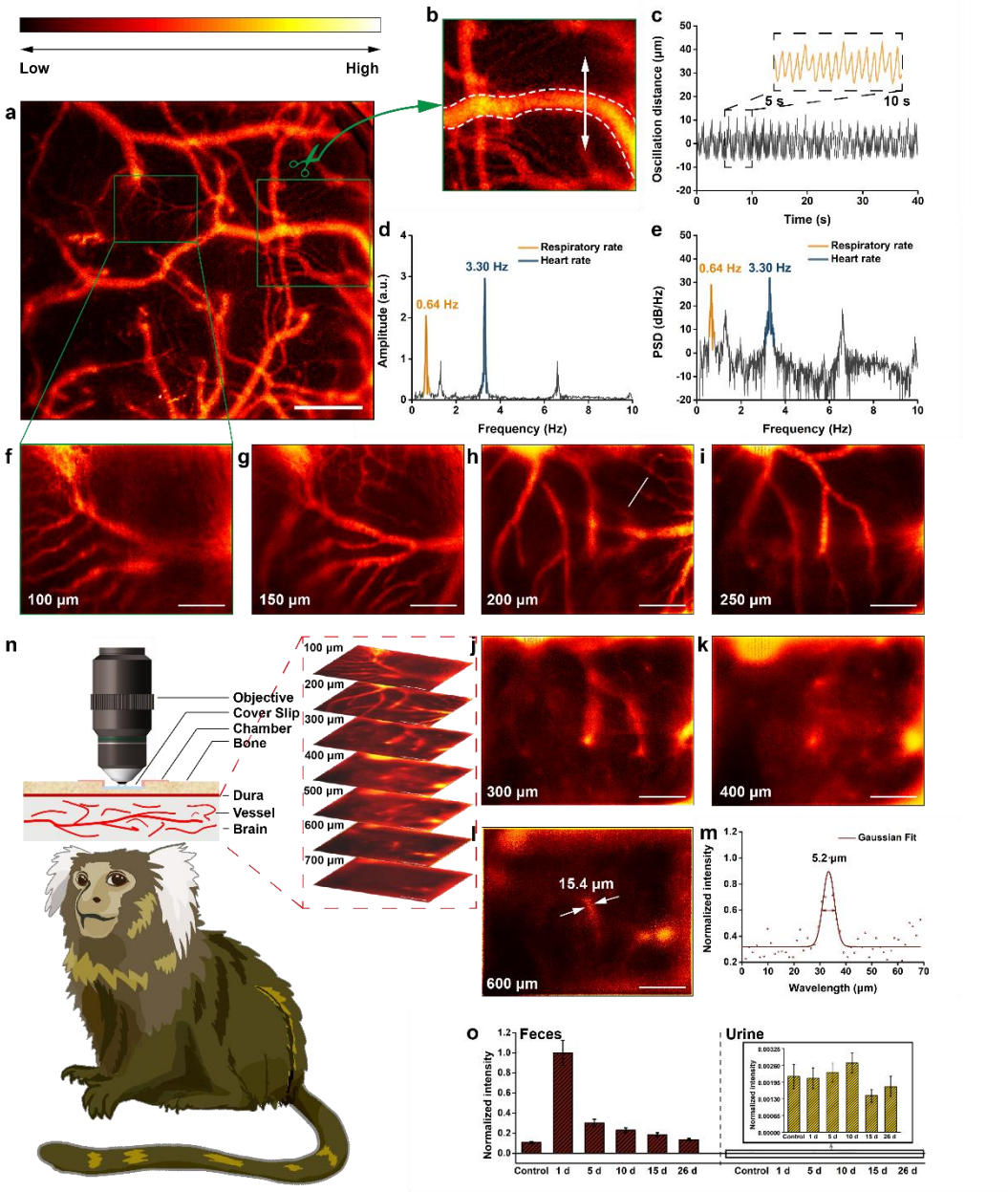

Fig. 3 | (a) A microscopic image (~5X) of brain vasculature. Scale bar, 300 μm. **(b)** The trembling of blood vessel. **(c)** The luminescence intensity of an inferior cerebral vein was plotted as a function of time. **(d)** The fast Fourier transformation of time-domain signals in **(c)**. **(e)** The power spectral density of **(c)**. **(d-e)** The calculation of the cardiac cycles **(b)** with a respiratory rate of 0.64 Hz and a heart rate of 3.30 Hz. **(f-i)** Images at various depth below the skull. Scale bar, 100 μm. **(j-l)** Images at various depth below the skull. Scale bar, 100 μm. **(m)** Cross-sectional fluorescence intensity profile along the white line of the cerebral blood vessel (inset of **Fig. 3h**). The Gaussian fit to the profile is shown in red line in **Fig. 3m**, which showed an extremely high spatial resolution. **(n)** The operation illustration of microscopic imaging. The skull of the marmoset was only thinned rather than opened, aiming at less minimal injury for bone regeneration. **(o)** The normalized P.L. intensity of the feces and urine from the

marmosets post intravenous injection of AIE dots (2 mg kg^{-1}).

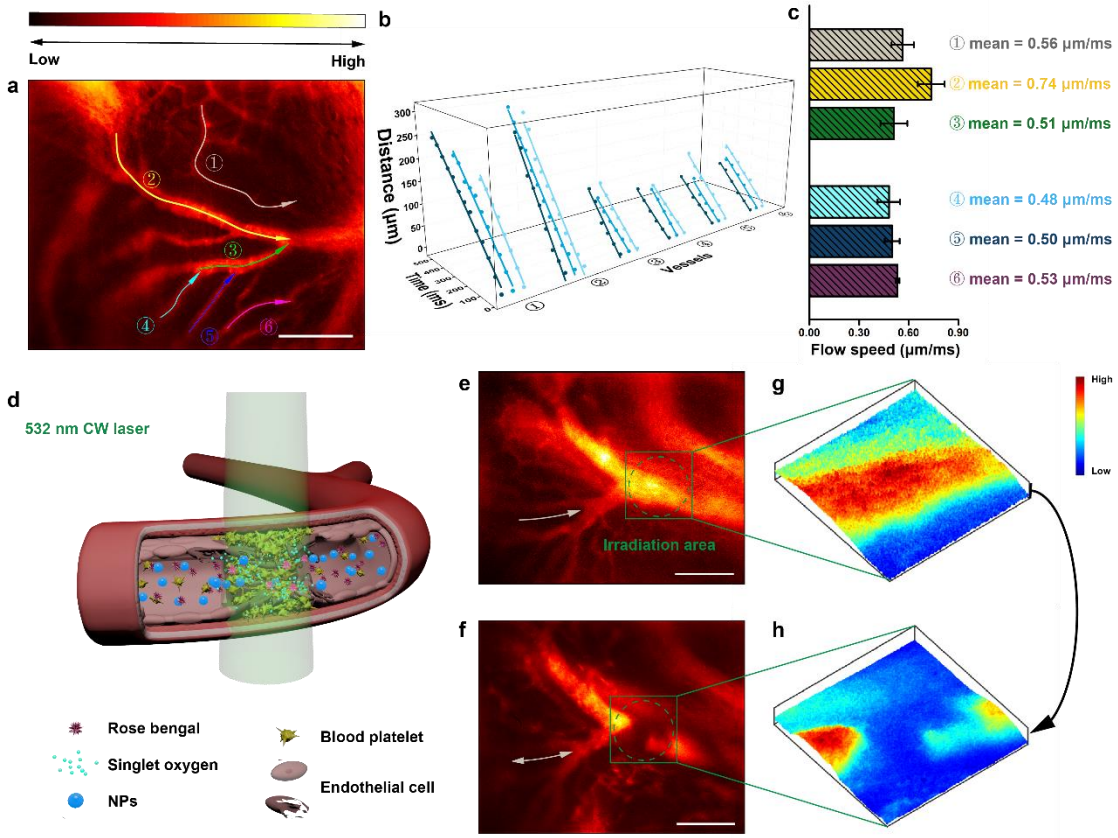

Fig. 4 | (a) A microscopic image (~25X) of brain vasculature and six vessels were selected. Scale bar, 100 μm. **(b)** The plots of positions of the point signal as a function of time (3 times) in the vessel 1-6 in **Fig. 4a**. **(c)** The mean rate of the vessel 1-6 in **Fig. 4a**. **(d)** Schematic illustration of PTI induction under excitation of CW 532 nm laser. **(e-f)** NIR-II fluorescence microscopic images of brain blood vessels before **(e)** and after **(f)** PTI induction. Scale bar, 100 μm. **(g-h)** 3D-intensity distributions of the irradiation area before **(g)** and after **(h)** PTI induction. The white arrows stand for the directions of flow before and after PTI induction. PTI induced the alteration of the blood flow direction.

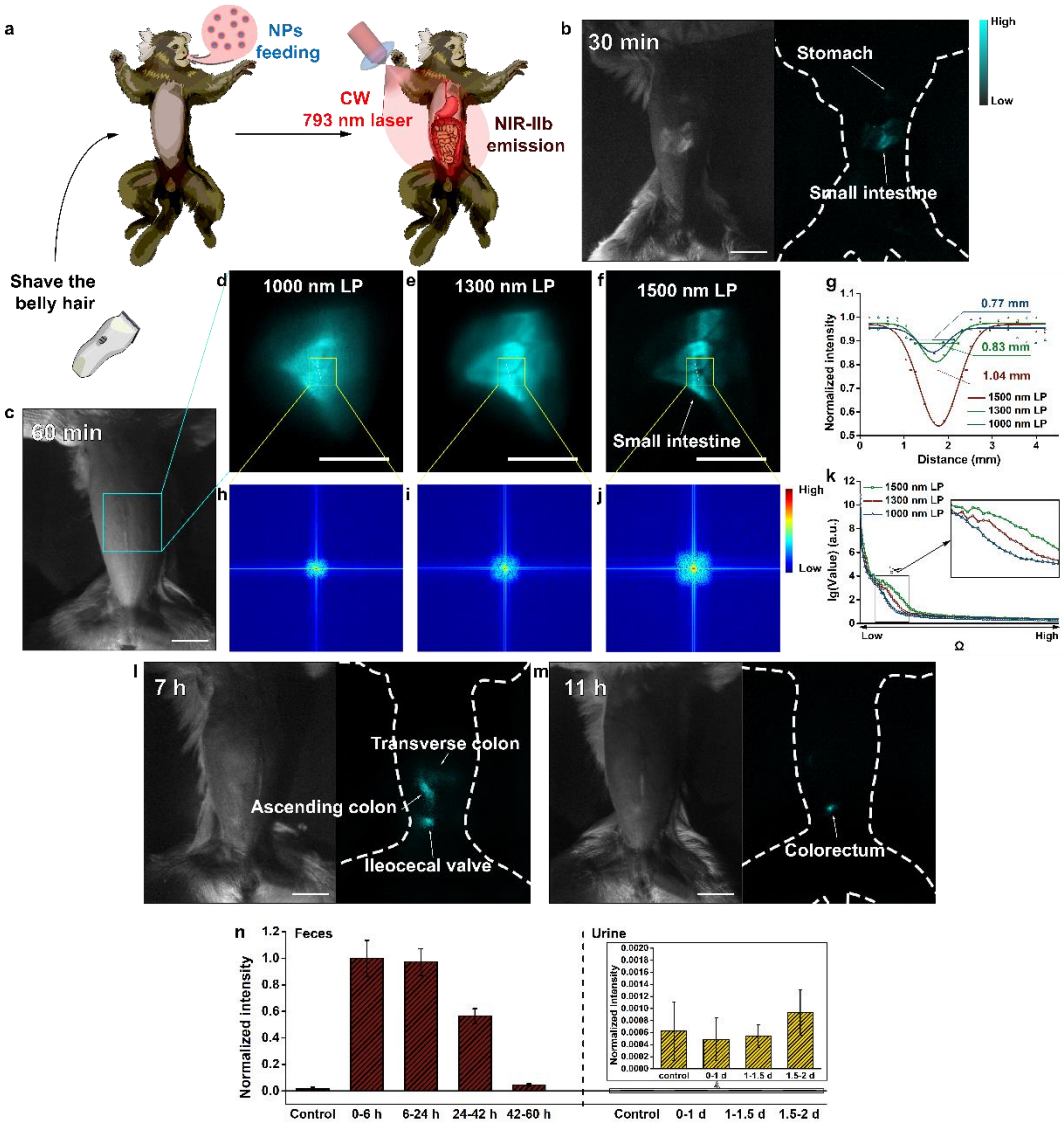

Fig. 5 | (a) The operation illustration of GI imaging. **(b)** The NIR-IIb fluorescence GI images at 30 min post feeding. **(c-f)** The NIR-II (beyond 1000 nm), NIR-IIa (beyond 1300 nm), NIR-IIb (beyond 1500 nm), fluorescence GI images at 60 min. **(g)** Cross-sectional fluorescence intensity profiles along the white line of the cerebral blood vessels (inset of **Fig. 5d-f**). **(h-j)** The FFT images of **(d-f)**. The Gaussian fit to the profile is shown in blue **(d),** green **(e)** and red **(f)** line in **Fig. 5g**. The NIR-IIb image showed better resolution capability. **(k)** The frequency distribution of **Fig. h-j**. The NIR-IIb image was confirmed to hold more high-frequency information. Scale bar, 20 mm. **(l-m)** The NIR-IIb fluorescence GI images at 7h and 11h post treatment. **(n)** The normalized P.L. intensity of the feces and urine from the marmosets post feeding of AIE dots (20 mg kg^{-1}). Scale bar, 20 mm.